



Effect of laser scanning angle and atmospheric oxygen on mechanical properties and microstructural morphology of selective laser-sintered aluminum-filled polyamide monolayers

Fernando J. Alamos¹ · Jorge A. Ramos-Grez^{1,2} · Loreto M. Valenzuela^{2,3}

Received: 15 February 2021 / Accepted: 15 April 2021 / Published online: 26 April 2021
© The Author(s), under exclusive licence to Springer-Verlag London Ltd., part of Springer Nature 2021

Abstract

The process parameters on selective laser sintering (SLS) have a strong effect on part quality. To better understand SLS of composite materials, this study focuses on the influence of laser scan angle and oxygen gas interaction on the mechanical properties, morphology, and joining mechanisms of laser-sintered aluminum-filled polyamide-12 single-layer specimens at room temperature. The results show that the strength and ductility increase with a higher laser scan angle (e.g., near 60°), and the oxygen concentration in the chamber shows a small effect on the elongation. No changes in the morphology and internal structure of the specimens were observed under a different set of process parameters. Additionally, two failure mechanisms were observed; a ductile failure that occurs when particles are well-blended where the metallic particles work effectively hindering crack propagations, and a brittle failure when local amounts of metallic particles are low.

Keywords Polyamide · Aluminum · Single-layer composite material · Selective laser sintering · Mechanical properties · Microstructural morphology

1 Introduction

Selective laser sintering (SLS) is an additive manufacturing (AM) process that can build complex 3D-shaped parts. It consists of a laser beam that selectively sinters layer by layer a bed of powder material. SLS has been used in many different applications in the automobile, aeronautics, biomedical, and artistic sectors [1–4]. SLS technologies have proven to

successfully print composite materials, which are extensively used in the polymer industry, especially when stiff and robust parts are required. The inclusion of fillers maintains the light-weight and ductile nature of polymers while adding stiffness to parts. Aluminum-reinforced polyamide blended powders have higher stiffness, thermal conductivity, and dimensional accuracy than unfilled polyamide [5] and can be used in SLS applications. They are typically used as non-safety-relevant parts in automotive components, wind tunnels, metallic molds for injection molding, and in biomedical components, such as medical devices and implants [5, 6].

The mechanical properties of printed SLS polyamide parts not only depend on the material powder used but are also influenced by several process parameters such as bed temperature, laser power, scan speed, scan spacing, layer thickness, delay time, and atmosphere [7]. Therefore, it is critical to understand the effects of the process parameters in part quality. Many studies have been conducted on the consolidation phenomenon that occurs in SLS and the influences of the printing parameters [8, 9]; however, there are still several printing parameter effects and interactions that are unknown due to the complexity of the process.

✉ Jorge A. Ramos-Grez
jramos@ing.puc.cl

¹ Department of Mechanical and Metallurgical Engineering, School of Engineering, Pontificia Universidad Católica de Chile, Santiago, Chile

² Research Center for Nanotechnology and Advanced Materials “CIEN-UC”, Pontificia Universidad Católica de Chile, Santiago, Chile

³ Department of Chemical and Bioprocess Engineering, School of Engineering, Pontificia Universidad Católica de Chile, Santiago, Chile

Previous efforts have studied how to improve the mechanical properties of SLS parts. Mazzoli et al. [10] characterized a new aluminum-filled polyamide powder developed for SLS application and compared the new material to a commercial polyamide powder. They concluded that the material maintains a considerable high-dimensional accuracy, strength and resistance to mechanical stress, and better finishing properties in comparison to the plain polyamide. They also reported that the aluminum-filled polyamide is an opaque material to the X-rays and therefore can be used in biomedical applications. Bassoli et al. [11] fabricated SLS specimens using an aluminum-filled polyamide and an alumina-polyamide composite material to investigate the mechanical properties and failure mechanisms and compare them with unfilled polyamide. They observed a strong anisotropy behavior, where the efficacy of the strengthening mechanisms during crack propagation depends on the printing direction: horizontal or vertical. Moreover, they observed that by modifying the scanning angle, enhanced mechanical properties can be achieved, results that were also reported by Stoia et al. [12]. Tarasova et al. [13] increased the aluminum content to 35%; however, they did not observe any enhancement in the flexural and tensile properties compared to commercially aluminum-filled polyamide powders. Bochnia and Blasiak [14] studied the rheological properties of aluminum-filled polyamide selective sintered parts, where material stress relaxation and creep models were developed and no significant differences were observed for parts built in different directions.

The effect of the atmospheric chemical composition inside the chamber during the SLS process of polymers has not been studied extensively in the literature. It is well known that the degradation of polymers exposed to air at high temperatures is essentially oxidative. In a previous study on injection molding, Nylon-6 and Nylon-66 yarns were exposed in air, nitrogen, or vacuum to temperatures from 136 to 215°C for periods from 5 min to 17.5 h. The ultimate tensile strength of the specimens was reduced by exposure to air [15]. A similar work studied the influence of degradation behavior of polyamide 12 (PA-12) powder for SLS at different building chamber temperatures and ambient conditions. The results showed that the processed material property melt volume and viscosity were reduced by storing the powder under vacuum during powder spreading [16]. Kummert et al. [17] used a thermoplastic elastomer material to analyze the aging effect caused by the temperature histories and oxygen atmosphere on the color and mechanical properties of printed specimens. The result revealed that a yellowish discoloration of the material depends on the temperature and the concentration of atmospheric oxygen. A higher discoloration was reached using an air atmosphere instead of a nitrogen atmosphere (0 vol.% oxygen content) and at higher temperatures. The mechanical properties of tensile strength and elongation did not change significantly when different atmospheres were used. In a more

recent study, Hariharan et al. [18] investigated the laser-material interaction of PA-12 powders, by comparing powder and sintered part properties. They concluded that the α polyamide crystalline structures are transformed to a γ structure due to the thermal exchange in the build chamber and the laser beam fuses together the powder particles at a particle boundary. Additionally, no element composition changes were reported due to the laser-material interaction. However, none of the previous works have attempted to study the oxidation effect of the laser beam on selective laser-sintered composite polymers, particularly those of metal-polymer origin.

The present study isolated the interaction between the laser energy density and oxygen concentration inside of the build chamber to analyze their effect on an aluminum-reinforced polyamide powder bed. The study was conducted without the effect of the high temperatures that SLS polymer powders commonly use. Instead, specimens were printed at room temperature and the effect of the laser energy density was assessed indirectly throughout the variation of the laser scan angle. The results showed the amount of oxygen in the chamber has a small effect on the mechanical properties of specimens printed at room temperature compared with the deleterious effect that temperature has on the SLS polymer part whenever oxygen is present. In part, this is thought to be a cause of the small interaction time the laser beam and oxygen atmosphere undergo with the powder bed.

2 Methodology

2.1 Experiment set-up and procedure

To study the degradation of aluminum-reinforced polyamide in SLS, a sealed chamber capable of varying the oxygen concentration was built and integrated into a laser scanning system. The experiment set-up is illustrated in Fig. 1a. The chamber (Fig. 1b) was capable of establishing a controlled atmospheric pressure from 0.2 to 6.0 bars at room temperature, which was connected to a mechanical vacuum pump and a pressurized argon line, and to generate a controlled atmosphere capable of holding different oxygen concentrations. A Nd:YAG fiberglass laser YLR-300-AC-MM from IPG Photonics corporation was used to sinter the powder that is placed inside of the chamber. The galvanometer's driven mirrors were controlled by a DE controller 3000 series from General Scanning Inc.

A commercial aluminum-reinforced polyamide 12 powder (Alumide EOS GmbH) was used in this study to laser sinter powder single-layer specimens. The printed specimens were designed using a CAD model that incorporated a fillet angle of 45°, and the size of the specimens was 4.1 mm in width and 56 mm in length. The oxygen content inside the chamber was varied at three different levels

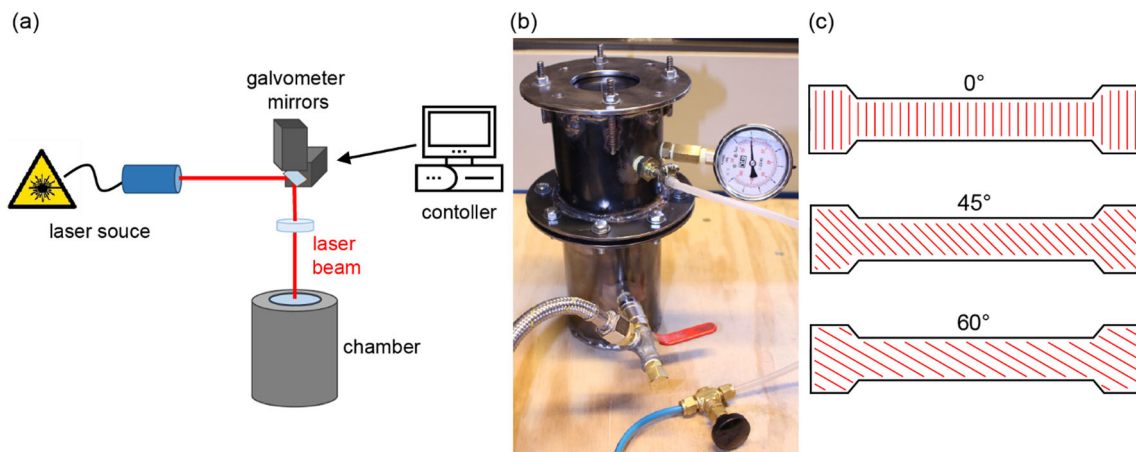


Fig. 1 a Experimental set-up schematic. b Chamber used to fabricate the specimens. c Scan angles (0°, 45°, and 60°)

(e.g., 0.51 vol.%, 3.2 vol.%, and nominal atmospheric conditions). For the specimens sintered at 0.51 vol.% and 3.2 vol.% oxygen, the gas pressure was first reduced to 0.2 bars (absolute) using a mechanical vacuum pump and then raised to the desired pressure using argon, diluting the percent of oxygen inside of the chamber. Positive pressure was held inside of the chamber to ensure that the surrounding air was not filtering inside. The percent of oxygen inside of the chamber (%vol.O₂) was estimated assuming an ideal gas law behavior and evaluating:

$$\%O_2 = \frac{P_i MW_{air} \%O_{2\ atm}}{P_i MW_{air} + (P - P_i) MW_{Ar}} \tag{1}$$

Where vol.%O_{2 atm} is the percent of oxygen on the atmosphere (20.95 vol.%), P_i is the initial pressure of the chamber (0.2 bar), P is the pressure, MW_{air} is the air molecular mass (29 g/mol), and MW_{Ar} is the molecular mass of argon (39.9 g/mol).

It is well known that the angle of the laser scan direction has an important effect on the mechanical properties. Three scanning angles (0°, 45°, and 60°) were used, shown in Fig. 1c, as a benchmark comparison of the effect on the mechanical properties between the oxygen concentration and the scan angle. Therefore, a 3² full factorial design with 8 replicas (72 total specimens) was implemented, where the oxygen concentrations inside the build chamber and laser scan angles were the modified factors. To achieve successful and testable specimens,

the printing parameters needed to be adjusted, which are shown in Table 1. It is important to highlight that the values used for the laser power, laser speed, and hatch distance are lower than typically used values for laser-sintered polyamide powders [19]; rendering a laser energy density (ED) of 2.8 J/mm² as commonly calculate elsewhere by the following expression,

$$ED = \frac{L_P}{L_s H_D}, \tag{2}$$

where L_P is the laser power, L_s is the laser speed, and H_D the hatch distance. This set of process parameters was calibrated in a previous study to achieve structurally sound single layers [20].

2.2 Characterization of the specimens

To characterize the effect of the oxygen content inside of the built chamber and the effect of the laser scan direction on the degradation of aluminum-reinforced polyamide parts sintered at room temperature, the mechanical properties, microstructural, and morphological characteristics of the printed specimens were studied.

Six replicas were tensile tested using a standard uniaxial tensile tester (Instron) with a 4900 N load cell and a crosshead speed of 1 mm/min to fracture. The ultimate tensile strength (UTS) and the elongation at fracture (e_f) were the measured responses. A caliper was used to measure the dimension of all

Table 1 Fixed printing parameters.

Fixed printing parameters	Values
Laser power (LP)	11 W
Laser speed (LS)	78 mm/s
Hatch distance (HD)	0.05 mm
Laser focus spot size	0.24 mm
Room temperature	17 °C

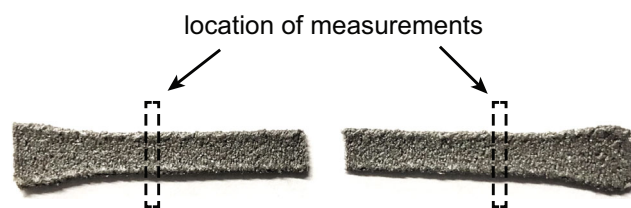


Fig. 2 Photograph of a specimen after tensile testing and the locations of the thickness and width measurements

the specimens. Average thickness and width measurements were calculated from two different locations on the specimen after tensile testing and far from the fracture, as is shown in Fig. 2. No significant distortions were observed far from the fracture section in specimens and both locations showed similar measured values.

The density of each specimen was measured applying the Archimedes' method. The latter were weighted under atmospheric conditions and then submerged in water. Equation 3 was used to calculate the densities of the specimens ρ ,

$$\rho = \frac{W_{\text{atm}} \rho_{\text{H}_2\text{O}}}{W_{\text{atm}} - W_{\text{H}_2\text{O}}}, \quad (3)$$

where $\rho_{\text{H}_2\text{O}}$ is the density of the water (1000 kg/m³), W_{atm} the weight of the specimen on the atmosphere, and $W_{\text{H}_2\text{O}}$ the weight in the water.

The porosity of each specimen was measured from the non-tensile-tested replicas, using a 3D density and geometry phantom evaluation procedure and a Micro CT 80 (Scanco Medical). The specimens were submerged in Dulbecco's phosphate-buffered saline contrast solution. The porosity of one specimen (i.e., printed angle 0° and under atmospheric conditions) was estimated to calibrate the parameters of the software used on the porosity assessment. To calculate the porosity of the reference specimen, the system of Eq. 4 through Eq. 6 was solved,

$$\rho = x \rho_{\text{PA}} + y \rho_{\text{Al}} + z \rho_{\text{air}} \quad (4)$$

$$x + y + z = 1 \quad (5)$$

$$\frac{y \rho_{\text{Al}}}{y \rho_{\text{Al}} + x \rho_{\text{PA}}} = 0.52 \quad (6)$$

where ρ is the density of the specimen, ρ_{PA} is the density of the PA-12 (1010 kg/m³), ρ_{Al} is the density of Al (2700 kg/m³), ρ_{air} is the density of the air (1.225 kg/m³), x is the volumetric percent of PA-12, y is the volumetric percent of the Al, z is the volumetric percent of the air of the specimen (porosity), and the weight percentage of Al in the material is 52% [11].

A scanning electron microscope (SEM) and an energy dispersive X-ray spectroscopy (EDS) were used to analyze a virgin Alumide powder sample and the printed specimens. The upper surface, bottom surface, and the cross-section of the fracture area of the tensile tested specimen were also observed under the microscope.

2.3 Data analysis

To quantify the effect that process parameters (laser scanning angle and oxygen concentration) have on the mechanical properties (UTS, e_f , and density), an analysis of variance (ANOVA) was performed for each response independently. The software Minitab 19 was used. The results were analyzed

with a 95% confidence interval. The ANOVA assumptions, independence of cases, homoscedasticity, and normality of the residuals, were met for all the analyses. The assumptions were checked with different residuals plots and using the Anderson-Darling test to verify the normality of the residuals [21].

3 Results

3.1 Tensile testing results

Figure 3 shows some examples of the stress-strain curves obtained from the tensile test. The slope of the curves slowly decreases, reaching a maximum strength, followed by a quick decay that ends with a fracture. This stress-strain curve shape is typically observed for 3-D printed polylactic acid (PLA) [22], polyamide, and aluminum-filled polyamide specimens [11].

The results for the UTS and e_f are shown in Fig. 4, and the p -values from the ANOVA test are shown in Table 2. The results show that the laser scanning angle is the only factor that has a significant effect (p -value < 0.05) on the UTS. As expected, an increase in the scanning angle causes an increase in the UTS, where the maximum value is at an angle of 60°. A similar result was also observed by Sabelle et al. [23] on individual Cu-Sn-Ni alloy metallic-sintered layers. An increase of 4.8% and 31.8% on the mean UTS is achieved using 45° and 60° laser scan angles, respectively, with respect to the samples printed at 0°. The oxygen concentration does not affect the UTS values, and it is clear that the error bars overlap between each other. The bigger variation on the mean values was only 0.4 MPa, while the standard deviations are at least 2.8 MPa.

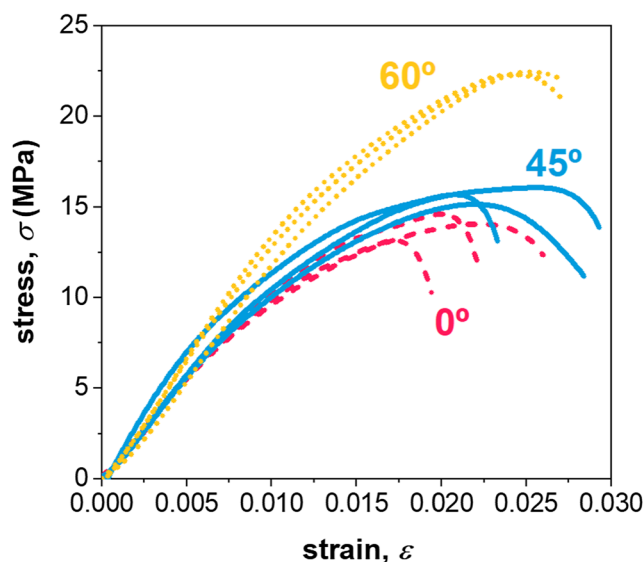


Fig. 3 Stress-strain curves for specimens printed with a laser energy density of 2.8 J/mm², nominal atmospheric conditions, and at 0°, 45°, and 60° laser scan angles

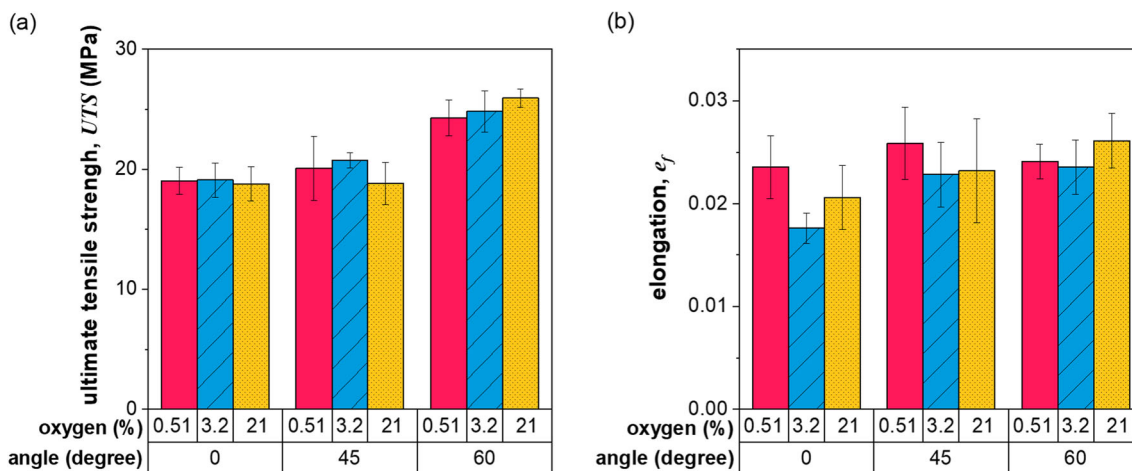


Fig. 4 a Ultimate tensile strength and b elongation at fracture at different laser scanning angles and oxygen concentrations inside the chamber

No influence on the UTS was observed from the interaction of the two factors.

For e_f both factors show a significant effect, although not their interaction (Table 2). The scanning angle has the largest influence. Figure 4b shows a significant increase from 0 to 45° but a smaller increase from 45 to 60°, with a total variation of 19.4% from 0 to 60°. For the oxygen level, it is observed an abrupt decrease of 13% in e_f between the specimens printed with a 0.5 vol.% and 3.2 vol.% oxygen level. However, the elongation increases when the oxygen level rises to 21 vol.%, and the difference in e_f is only 9.2% between the specimens printed at 3.2 vol.% oxygen and nominal atmospheric conditions. Therefore, these results suggest that the oxygen level may play a small effect on the elongation.

3.2 Density and porosity results

Figure 5 shows the results of the density and porosity of the printed parts. No important changes were found by varying the laser scanning angle and the oxygen concentration, neither from the plots nor the ANOVA test results. A different scan angle will modify the printed pattern but will not affect the energy density distribution which plays a major role in the densification of the parts. Therefore, no variations in density were expected, nor in porosity since they are correlated.

Table 2 P-values for ultimate tensile strength (UTS) and elongation at fracture from the ANOVA test

Model terms	UTS	Elongation
Angle	< 0.001	0.001
%Oxygen	0.669	0.012
Angle × %Oxygen	0.118	0.146
R^2	78.8%	43.4%

3.3 Morphology

The EOS Alumide powder is a mixture of PA-12 and Al particles, where the particle size range is between 30 and 250 μm (Fig. 6). The PA-12 particles have a spherical shape, are rougher than the Al particles, and are principally composed of carbon, iridium, oxygen, and nitrogen (hydrogen could not be measured by the EDS probe). The Al particles instead show an extended shape, are smoother, and have a thin Al₂O₃ surface layer.

A scanning electron microscopy (SEM) was used to analyze both the cross-section at the fractured area after the tensile testing and the upper and bottom surfaces of the specimens. No differences were found in the morphology between the specimens, and all of them show similar characteristics. Two distinct areas can be differentiated in the specimens as shown in Fig. 7, where Al particles are submerged within a polyamide matrix. The melting temperature for the PA-12 is 176 °C [5] and for Al is closed to 660 °C. The laser beam increases the temperature of the powder enough to melt the polyamide and heat the Al particles, creating a melt pool. Then the melted polyamide starts to flow, filling the gaps between the Al particles and surrounding them, generating a strong and dense part. Similar joining mechanisms have been reported for laser-sintered glass-filled polyamide bars [24, 25]. Two failure mechanisms were identified in different regions of the specimens, due to signs of the strain of the polyamide. Firstly, a ductile failure can be observed in Fig. 7a and b. The ductile failure occurs in large areas at the middle of the specimens, where the Al particles emerged from a deformed, stretched, and torn polyamide matrix. Secondly, brittle failure zones were identified at different areas of the specimens (Fig. 7a and c) where the polyamide fails without signs of being stretched, yet rather being cut through.

Three different regions with distinctive characteristics and morphology were recognized on the specimens: a top, a middle, and a bottom region. The top region consists of a thinner layer

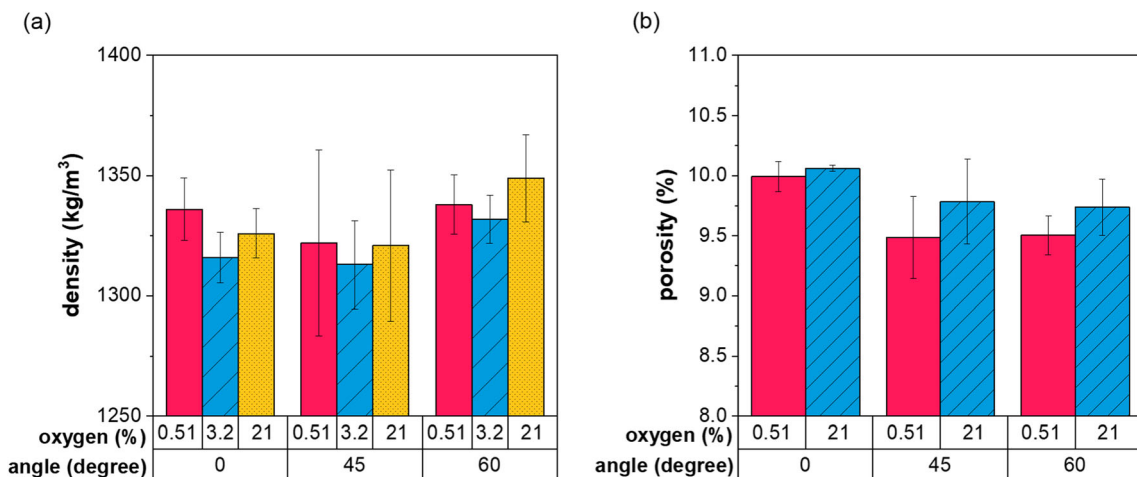


Fig. 5 a Density and b porosity for specimens printed with different laser scanning angles and oxygen level inside of the built chamber

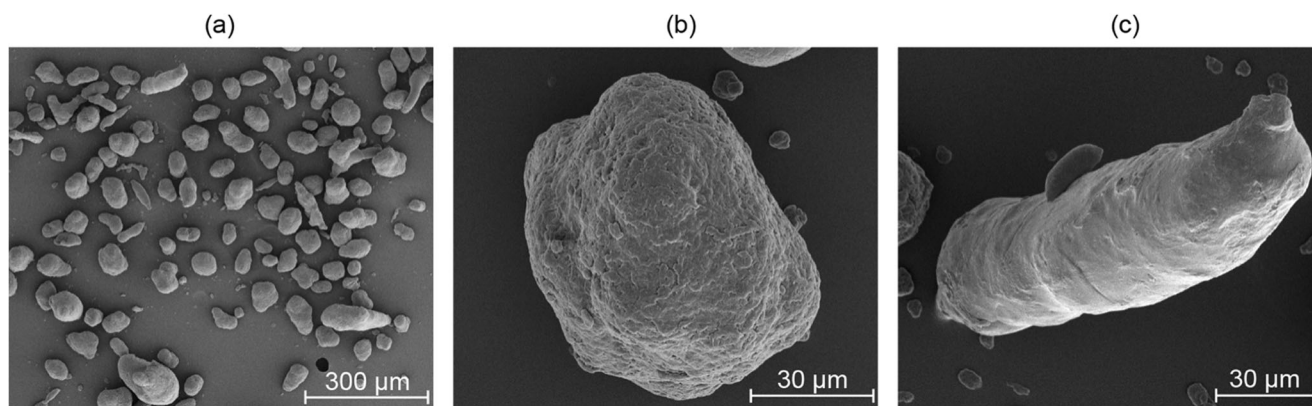


Fig. 6 SEM images of Alamide powder. a Virgin powder sample (250×). b PA-12 particle (2500×). c Al particle (2000×)

of polyamide due to the differences in specific weight between the polyamide and Al particles (Fig. 8a). The PA-12 is a semi-crystalline polymer, and amorphous zones and spherulites were identified on the top surface of the specimens (Fig. 9). Spherulites correspond to a spherical packing of polymeric

chains whose morphology under the microscope is evident. The middle region of the specimens is the most extended area and is formed by Al particles submerged within a polyamide matrix. Two different failure zones were identified in this region: a ductile failure zone where Al particles are well

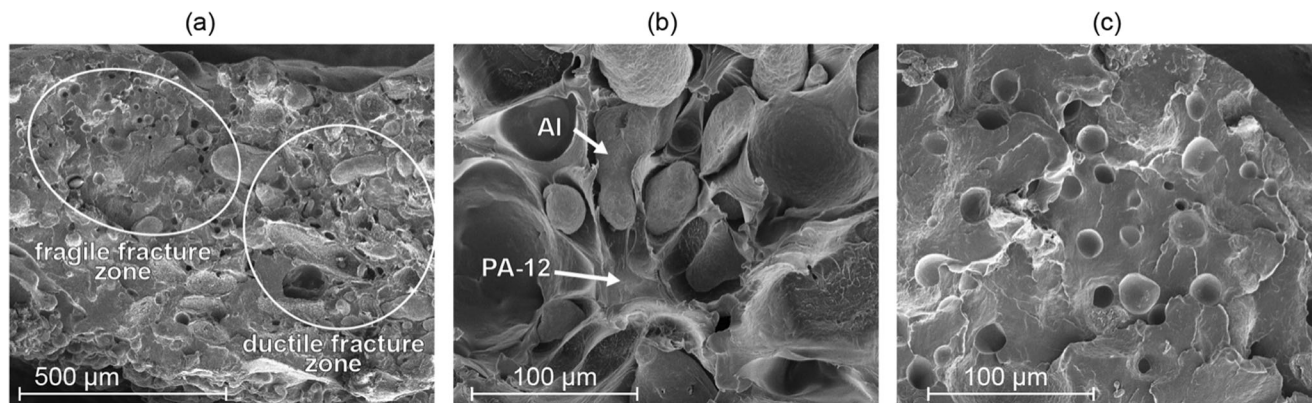
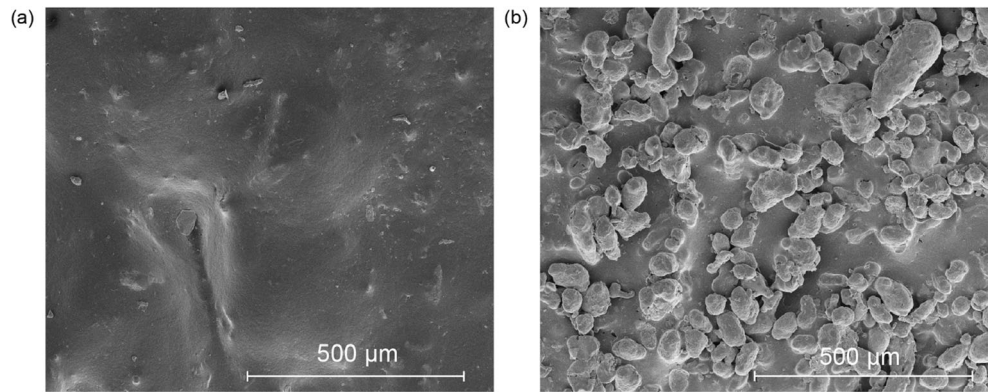


Fig. 7 Micrographs at the fractured surface. a Overall view of a specimen printed at 21 vol.% oxygen, and 0° scan angle showing ductile and brittle fracture zones (250×). b Ductile fracture zone at the middle of the

specimens of specimen printed at 0.5 vol.% oxygen, and 0° scan angle (1000×). c Brittle fracture zone at the top of a specimen printed at 21% oxygen, and 0° scan angle (1000×)

Fig. 8 Micrographs of the overall surface views of the specimens. **a** Top surface of a specimen printed at 21 vol.% oxygen, and 60° scan angle (250×). **b** Bottom surface of a specimen printed 21 vol.% oxygen, and 60° scan angle (250×)



distributed and a brittle failure zone where there is an absence of Al particles due to the coagulation of polyamide particles. The bottom region is formed by a mixture of Al and polyamide particles adhered to the melted polyamide matrix (Fig. 8b). The morphology in this region presents a larger number of voids, higher porosity, and higher surface roughness. Figure 10 illustrates an example of an unmelted polyamide particle adhered to the melted polyamide matrix. Interface detachment between the PA-12 sphere and melted matrix is observed.

3.4 Microtomography

A 3D density and geometry phantom evaluation procedure using a micro-CT was used to analyze the internal structure and measure the porosity of the no tensile tested specimens. Figure 11a shows the cross-section analysis of a specimen. No significant differences were found for specimens printed at different oxygen levels with the same laser scan angle, which confirms the results observed for the density. The internal

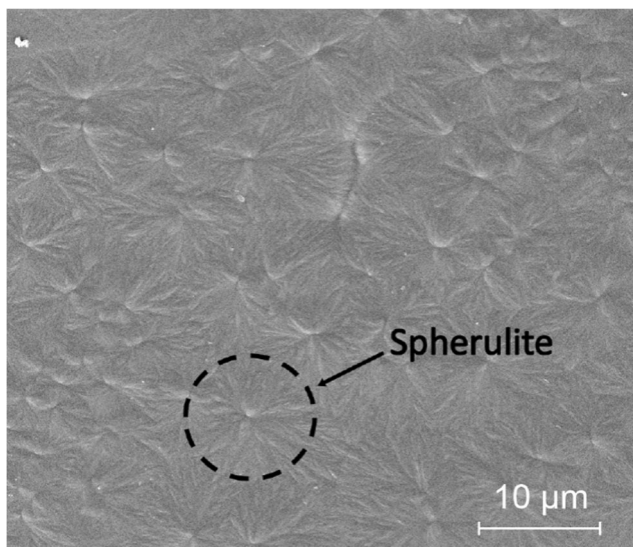


Fig. 9 Micrograph on the top surface of a specimen showing spherulites formation on the polyamide matrix having a diameter near to 10 μm. Specimen printed at 21 vol.% oxygen, and 60° scan angle (5000×)

structure of the specimen is revealed in Fig. 11b, where important amounts of voids and pores are observed inside.

Warping had a considerable effect on all the specimens, generating a curved shape that can be noticed in the cross-section images (Fig. 11). The melting point of the polyamide is around 176 °C; however, the ambient temperature was 20 °C and no heating was implemented during the laser sintering process. Because of this, a high-temperature difference between the single-layer and the surrounding atmosphere exists, and heat transfer via radiation and convection predominates. The top surface of the bar cools down faster than the bottom surface during the solidification process. This generates a significant thermal gradient across the thickness which can warp the specimens due to residual stresses accommodation.

The laser scanning angle effect can be noticed on the specimens in Fig. 12. During the laser beam scanning process, the melt pool creates a scanning trail; therefore, different scanning angles generate distinct paths in the specimens. Using a scan angle of 0°, horizontal lines across the specimens were observed. Inclined lines are observed for specimens printed at 45° and 60°, and the thickness of the specimen oscillates

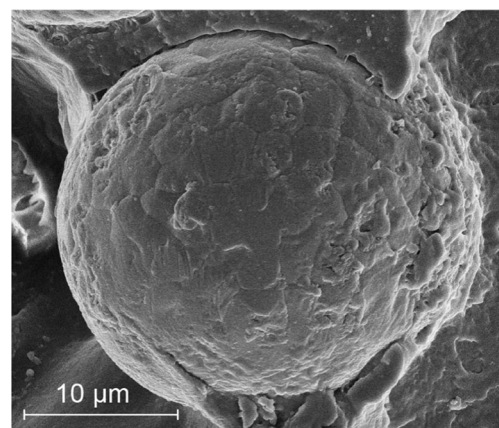


Fig. 10 Micrograph at the bottom area of the fractured surface showing an unmelted PA-12 particle adhered and surrounded by melted PA-12. Specimens printed 21 vol.% oxygen, and 60° scan angle (8000×)

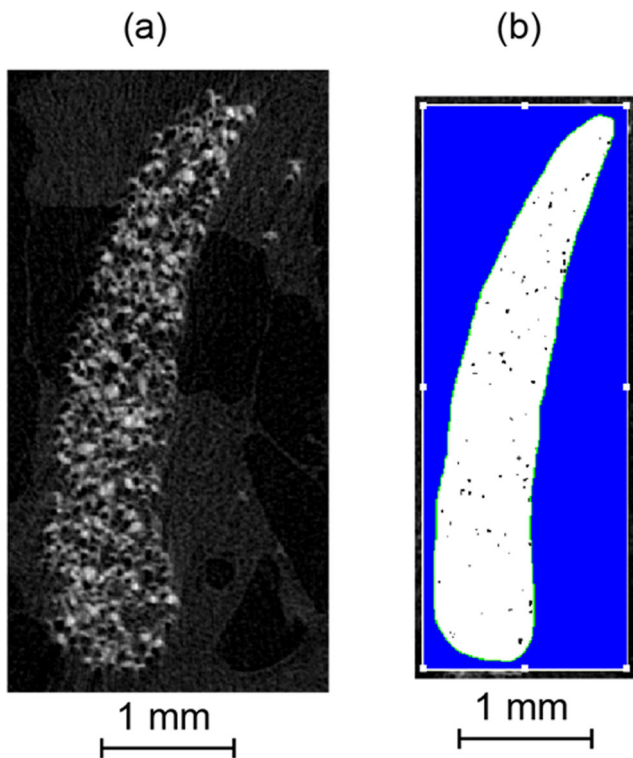


Fig. 11 **a** Micro CT cross-section image of a specimen printed at 0.5 vol.% oxygen, and 60° scan angle and its **b** phantom evaluation image

through the cross-section according to the inclination of the path lines. Additionally, the inner pores and the surfaces of all specimens were also observed.

4 Discussion

Sintering at room temperature creates high residual stresses on the parts due to the abrupt temperature gradient while cooling.

For SLS polymers parts, warping typically occurs due to the residual stresses, an observed phenomenon in the printed parts of this study. This was done on purpose, to isolate the effect of the laser energy density and the oxygen concentration inside the chamber on the aluminum-reinforced polyamide powder.

As expected, the laser scan angle affected the ultimate tensile strength (UTS) and elongation at fracture (e_f), but not in the density and porosity since the applied energy density is the same. On the other hand, oxygen has a small effect on the elongation to fracture but not in the rest of the assessed properties. Therefore, the atmospheric oxygen in the chamber has a small effect on the oxidation and degradation of the powder bed only when and where the laser beam is scanned. A possible explanation would be on the powder composition; the Al particles showed an Al_2O_3 passivating surface layer, and the beam energy is not enough to melt them, as is shown in Fig. 7c. Therefore, no oxidation effect can be assumed for the Al particles since the external layer is already oxidized. For the polyamide particles, there is important interaction with the laser since they melt; however, the sintering process time is so short that it may be the reason why no important oxidation occurs. Nonetheless, high temperature causes thermal oxidation in polyamides. Thermal oxidation in PA-6 and PA-12 increases the crystallinity of the polymer, which caused an important decrease in the elongation to break of the material. The crystallinity increases because oxygen molecules and elevated temperatures may cause chain cleavage reactions in the amorphous phase of the polyamide and additional mobile chains are produced that might become part of the polymeric crystallites [26–28]. Additionally, chain scission of polyamide occurs at long times under oxygen, while cross-linking is the dominant effect during the printing process [16]. Thus, any major contribution may be caused by a higher temperature preheat at longer time scales [29].

The two different failure mechanisms, ductile and brittle, observed in the specimens are explained by the stiffness difference of both materials and the distribution of the particles across the

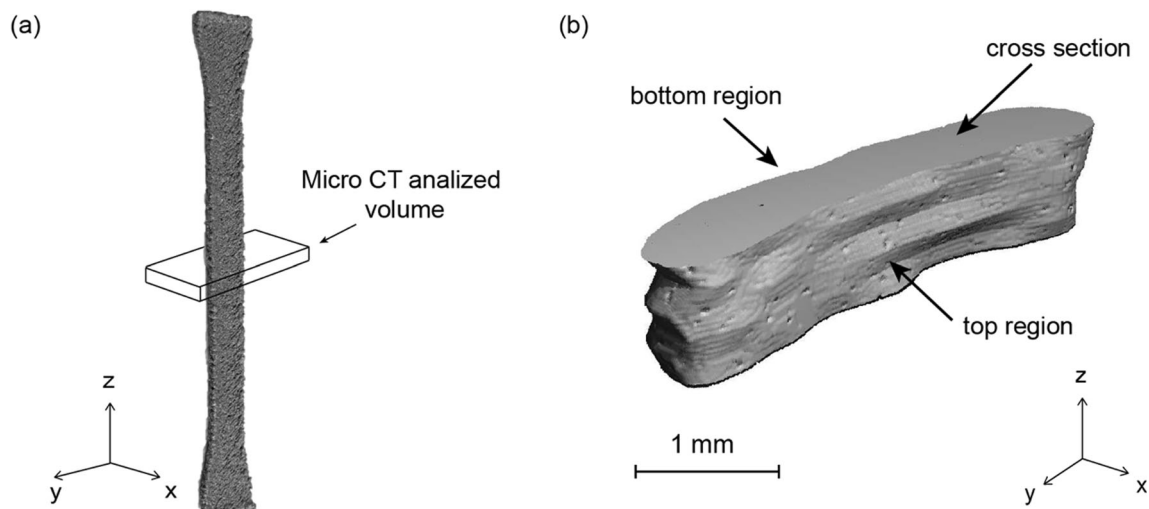


Fig. 12 **a** Picture of a specimen printed with 0.5 vol.% oxygen at 0° scan angle and **b** its 3-D micro-CT image analyzed volume

specimen. Al has a considerably higher strength than the polyamide; therefore, failure only occurs only in the polyamide matrix, which is clear in Fig. 7b. In well-blended areas, the distribution of the Al particles shows effectiveness in blunting crack propagations through the polyamide, which leads to the polyamide yielding and causes a ductile fracture. Ductile zones were the most common in this region among the specimens, and therefore is the predominant failure mechanism, which explains the shape of the stress-strain curves shown in Fig. 3. Bassoli et al. [11] observed similar failure mechanisms on laser-sintered aluminum-filled polyamide multilayer bars. However, for poorly blended areas, the concentration of Al particles is low, and cracks can easily propagate without any obstruction which causes a brittle failure. It has been reported in previous research that aluminum-reinforced polyamide powder often shows coagulation because the mixing process is not always effective due to the difference in size and density of the particles and electrostatic forces [8]; this may be the reason why poor-blended areas are formed. Figure 7c shows an amplification of the brittle failure zone in Fig. 7a, where it can be seen that no Al particles are present in that zone due to the coagulation of the polyamide particles.

A solid dense layer of molten polyamide is formed on the top specimens. Al is denser than polyamide; therefore, when the polyamide particles melt the Al particles sink and form a top layer of polyamide. This phenomenon can be seen clearly in Fig. 8a, where all Al particles are covered by a layer of melted polyamide. Additionally, spherulites were found on the top layer of molten polyamide (Fig. 8b). The formation of spherulites occurs during the cooldown of the polymer by slow and controlled recrystallization of the polyamide after the scanning of the laser beam, which creates the spherulite core by primary nucleation, followed by the radial growth of fibrillar crystals at a constant rate. Spherulites regions are typically more densely packed than in the amorphous phase of the polymer; therefore, some mechanical properties like density, tensile strength, and Young's modulus increase in those regions [30, 31].

The morphology of the bottom region of the specimens is a mixture of Al and polyamide particles adhered to the melted polyamide matrix and is explained by the phenomenon of the melt pool. A lower energy density reaches the bottom of the layer, and there is not enough energy to melt through the polyamide composite powder layer. Therefore, the powder particles joined to the melted polyamide on the top.

Finally, through micro-CT observation, an important quantity of voids and pores can be appreciated inside of the specimens (Fig. 11b). The porosity occurs during the consolidation process. Due to the different sizes of the particles, gaps between the particles exist. When the polyamide particle is melted, the polyamide starts to flow between the Al particles; however, since the melted polymers have high viscosity, not

all the gaps are filled, and voids and traps remain in the solid part. The average porosity of the specimens was 9.8%. It is important to notice that this reduces the effective cross-section and the tensile strength of objects.

5 Conclusions

The following conclusions can be made based on this research:

- The oxygen concentration inside the chamber does not affect the ultimate tensile strength, density, and porosity of SLS parts. Only a small effect on the elongation to fracture was noticed.
- The oxidation of the polyamide and Al does not predominate during the laser—oxygen—powder bed interaction.
- The scanning angle was modified between 0°, 45°, and 60°, the latter rendering the best mechanical properties. As expected, the density of the layers did not change with different scan angles.
- A morphology analysis revealed a composite structure formed by filled-reinforcement Al particles submerged within a molten polyamide matrix. The Al particles effectively work against crack propagation during tensile testing, leading to ductile fracture of the specimens.

These results have important consequences for aluminum-filled polyamide selective laser-sintered parts production, since it has been proved that the thermal oxidation caused by the laser beam on the powder bed has a small impact on the mechanical properties and a better understanding of the failure mechanism has been provided, findings that are relevant for part design and quality.

Acknowledgements Gratitude is extended to DICTUC SA for the technical support in the design and build of the chamber and tensile testing, and Dr. Glen Niebur and Dr. Steven Schmid for access to the Micro CT and laboratory facilities at the University of Notre Dame.

Author's contribution Fernando J. Alamos: original idea of the paper, literature review, design of experiments, experimental setup, data generation: microstructural evaluation, tensile testing, analysis of variance, manuscript writing. Jorge Andrés Ramos-Grez: original conceptualization of the paper, close supervision, and guidance during the research process, critical advice, data generation: scanning electron microscopy and energy-dispersive spectroscopy data collection, manuscript proofreading, and funding. Loreto M. Valenzuela: literature review, critical advice, and manuscript proofreading.

Funding The authors received financial support from the University of Notre Dame and Pontificia Universidad Católica de Chile (UND-PUC) Seed Fund for the SEM and EDS electronic microscope analysis, and from ANID FONDECYT project #1201068.

Declarations

Ethical approval Not applicable.

Consent to participate All the authors involved have agreed to participate in this submitted article.

Consent for publication All the authors involved in this manuscript give full consent for publication of this submitted article.

Competing interests The authors declare no competing interests.

References

- Bernard A, Taillandier G, Karunakaran KP (2009) Evolutions of rapid product development with rapid manufacturing: concepts and applications. *Int J Rapid Manuf* 1:3–18. <https://doi.org/10.1504/IJRAPIDM.2009.028929>
- Negi S, Dhiman S, Sharma RK (2013) Basics, applications and future of additive manufacturing technologies: a review. *J Manuf Technol Res* 5:75–96
- Negi S, Sharma RK, Dhiman S (2014) Experimental investigation of SLS process for flexural strength improvement of PA-3200GF Parts. *Mater Manuf Process* 30:644–653. <https://doi.org/10.1080/10426914.2014.994750>
- Kalpakjian S, Schmid S (2014) *Manufacturing engineering and technology*, 7th edn. Pearson, Boston
- EOS GmbH (2012) Alumide data sheet
- Tiwari SK, Pande S, Agrawal S, Bobade SM (2015) Selection of selective laser sintering materials for different applications. *Rapid Prototyp J* 21:630–648. <https://doi.org/10.1108/RPJ-03-2013-0027>
- Goodridge RD, Tuck CJ, Hague RJM (2012) Laser sintering of polyamides and other polymers. *Prog Mater Sci* 57:229–267. <https://doi.org/10.1016/j.pmatsci.2011.04.001>
- Kruth JP, Levy G, Klocke F, Childs THC (2007) Consolidation phenomena in laser and powder-bed based layered manufacturing. *CIRP Ann Manuf Technol* 56:730–759. <https://doi.org/10.1016/j.cirp.2007.10.004>
- Caulfield B, McHugh PE, Lohfeld S (2007) Dependence of mechanical properties of polyamide components on build parameters in the SLS process. *J Mater Process Technol* 182:477–488. <https://doi.org/10.1016/j.jmatprotec.2006.09.007>
- Mazzoli A, Moriconi G, Pauri MG (2007) Characterization of an aluminum-filled polyamide powder for applications in selective laser sintering. *Mater Des* 28:993–1000. <https://doi.org/10.1016/j.matdes.2005.11.021>
- Bassoli E, Gatto A, Iuliano L (2012) Joining mechanisms and mechanical properties of PA composites obtained by selective laser sintering. *Rapid Prototyp J* 18:100–108. <https://doi.org/10.1108/13552541211212087>
- Stoia DI, Linul E, Marsavina L (2019) Influence of manufacturing parameters on mechanical properties of porous materials by selective laser sintering. *Materials (Basel)* 12:871. <https://doi.org/10.3390/ma12060871>
- Tarasova A, Wegner A, Witt G (2019) Approach to defining the maximum filler packing volume fraction in laser sintering on the example of aluminum-filled polyamide 12. In: 30th Annual International Solid Freeform Fabrication Symposium—An Additive Manufacturing Conference. pp 977–986
- Bochnia J, Blasiak S (2020) Stress relaxation and creep of a polymer-aluminum composite produced through selective laser sintering. *Polymers (Basel)* 12:830. <https://doi.org/10.3390/polym12040830>
- Valkot EI, Chiklis CK (1965) Effects of thermal exposure on the physicochemical properties of polyamides. *J Appl Polym Sci* 9:2855–2877. <https://doi.org/10.1002/app.1965.070090820>
- Wudy K, Drummer D, Kühnlein F, Drexler M (2014) Influence of degradation behavior of polyamide 12 powders in laser sintering process on produced parts. *AIP Conf Proc* 1593:691–695. <https://doi.org/10.1063/1.4873873>
- Kummert C, Josupeit S, Schmid H-J (2017) Thermoplastic elastomer part color as function of temperature histories and oxygen atmosphere during selective laser sintering. *J Miner Met Mater Soc* 70:425–430. <https://doi.org/10.1007/s11837-017-2658-2>
- Hariharan K, Arumaikkannu G, Ramkumar T, Selvakumar M (2020) Material stability investigation of polyamide material before and after laser sintering. *Int J Polym Anal Charact* 25:158–165. <https://doi.org/10.1080/1023666X.2020.1766798>
- Zarringhalam H, Hopkinson N, Kamperman NF, de Vlieger JJ (2006) Effects of processing on microstructure and properties of SLS Nylon 12. *Mater Sci Eng A* 435–436:172–180. <https://doi.org/10.1016/j.msea.2006.07.084>
- Alamos Domeyko FJ (2018) Effect of scanning direction, atmospheric oxygen and laser power on mechanical properties of selective laser sintering (SLS) of aluminum-filled polyamide monolayers. *Pontificia Universidad Católica de Chile*
- Montgomery DC (2012) *Design and analysis of experiments*, Eight edn. Wiley, Hoboken
- Kim H, Park E, Kim S et al (2017) Experimental study on mechanical properties of single- and dual-material 3d printed products. *Procedia Manuf* 10:887–897. <https://doi.org/10.1016/j.promfg.2017.07.076>
- Sabelle M, Walczak M, Ramos-Grez J (2018) Scanning pattern angle effect on the resulting properties of selective laser sintered monolayers of Cu-Sn-Ni powder. *Opt Lasers Eng* 100:1–8. <https://doi.org/10.1016/j.optlaseng.2017.06.028>
- Negi S, Dhiman S, Sharma RK (2015) Determining the effect of sintering conditions on mechanical properties of laser sintered glass filled polyamide parts using RSM. *Meas J Int Meas Confed* 68:205–218. <https://doi.org/10.1016/j.measurement.2015.02.057>
- Negi S, Dhiman S, Sharma RK (2014) Basics and applications of rapid prototyping medical models. *Rapid Prototyp J* 20:256–267. <https://doi.org/10.1108/RPJ-07-2012-0065>
- Pavlov NN, Kudryavtseva GA, Abramova IM, Vasil'eva VA, Zezina LA, Kazaryan LG (1987) Physical transformations and change in mechanical properties on thermal ageing of aliphatic polyamides. *Polym Sci USSR* 29:967–973. [https://doi.org/10.1016/0032-3950\(87\)90477-1](https://doi.org/10.1016/0032-3950(87)90477-1)
- Dong W, Gijsman P (2010) Influence of temperature on the thermo-oxidative degradation of polyamide 6 films. *Polym Degrad Stab* 95:1054–1062. <https://doi.org/10.1016/j.polymdegradstab.2010.02.030>
- Su KH, Lin JH, Lin CC (2007) Influence of reprocessing on the mechanical properties and structure of polyamide 6. *J Mater Process Technol* 192–193:532–538. <https://doi.org/10.1016/j.jmatprotec.2007.04.056>
- Josupeit S, Schmid HJ (2017) Experimental analysis and modeling of local ageing effects during laser sintering of polyamide 12 in regard to individual thermal histories. *J Appl Polym Sci* 134. <https://doi.org/10.1002/app.45435>
- Carraher CE (2003) *Polymer chemistry*, Sixth edn. Marcel Dekker, Inc, New York
- Crist B, Schultz JM (2016) Polymer spherulites: a critical review. *Prog Polym Sci* 56:1–63. <https://doi.org/10.1016/j.progpolymsci.2015.11.006>

Publisher's note Springer Nature remains neutral with regard to jurisdictional claims in published maps and institutional affiliations.